
Article:

Smyl, D., Rashetnia, R., Seppanen, A. et al. (2017) Can Electrical Resistance Tomography be used for imaging unsaturated moisture flow in cement-based materials with discrete cracks? Cement and Concrete Research, 91. pp. 61-72. ISSN: 0008-8846

https://doi.org/10.1016/j.cemconres.2016.10.009

Can Electrical Resistance Tomography be used for imaging unsaturated moisture flow in cement-based materials with discrete cracks?

Danny Smyl[a], Reza Rashetnia[a], Aku Seppänen[b], Mohammad Pour-Ghaz[a,1,*]

[a]*Department of Civil, Construction, and Environmental Engineering, North Carolina State University, Raleigh, NC*
[b]*Department of Applied Physics, University of Eastern Finland, Kuopio, Finland*

Abstract

Previously, it has been shown that Electrical Resistance Tomography (ERT) can be used for monitoring moisture flow in undamaged cement-based materials. In this work, we investigate whether ERT could be used for imaging three-dimensional (3D) unsaturated moisture flow in cement-based materials that contain discrete cracks. Novel computational methods based on the so-called absolute imaging framework are developed and used in ERT image reconstructions, aiming at a better tolerance of the reconstructed images with respect to the complexity of the conductivity distribution in cracked material. ERT is first tested using specimens with physically simulated cracks of known geometries, and corroborated with numerical simulations of unsaturated moisture flow. Next, specimens with loading-induced cracks are imaged; here, ERT reconstructions are evaluated qualitatively based on visual observations and known properties of unsaturated moisture flow. Results indicate that ERT is a viable method of visualizing 3D unsaturated moisture flow in cement-based materials with discrete cracks.

Keywords: Crack Detection, Finite Element Analysis, Image Analysis, Mortar, Transport Properties

---

1. Introduction

The resistance of concrete structures to the ingress of moisture and aggressive ions is commonly considered a measure of their durability [1, 2]. Cracking creates preferential pathways for moisture and aggressive ions to penetrate the bulk material and decrease the durability of concrete structures [3, 4, 5]. To understand the role of cracks in moisture flow, and durability in general, imaging methods are needed.

Several imaging methods that exploit electromagnetic radiation have been used to study moisture movement in concrete and other cement-based materials with discrete cracks. Roels et al. [6] used 2D X-ray radiography to monitor moisture penetration in brick with discrete cracks to validate moisture flow simulations. Roels and Carmeliet [7] later used a 2D X-ray radiography technique to study homogeneous and non-homogeneous material with micro-scale discrete cracks. Pour-Ghaz et al. [8, 9] corroborated numerical simulations of unsaturated moisture flow with 2D X-ray radiography to assess moisture movement in a saw-cut. Kanematsu et. al [10] used neutron radiography to image moisture flow in bending-induced cracks; they showed that the moisture content of the cementitious materials surrounding the cracks significantly affects the rate of moisture ingress. Carmeliet et al. [11] measured crack distribution in concrete using 3D microfocus X-ray Computed Tomography (CT) and monitored water distribution resulting from infiltration of water in a variable aperture crack. Fukuda et al. [12] investigated self-healing of cracks in low-permeability concrete using X-ray CT imaging. Recently, Li et al. [13] used neutron radiography to monitor water uptake in simulated concrete pavement joints, showing that entrained air saturates more slowly than the gel porosity. These examples demonstrate that cracking and moisture movement in cementitous material (and porous material, in general) can be captured using imaging modalities based on electromagnetic radiation.

---

[*] Corresponding author
Email address: `mpourghaz@ncsu.edu` (Mohammad Pour-Ghaz)
[1] Campus Address: North Carolina State University, Department of Civil, Construction, and Environmental Engineering, Campus Box 7908, 431C Mann Hall, Raleigh, NC 27695-7908

Preprint submitted to Cement and Concrete Research *September 4, 2016*

Moreover, imaging based on electromagnetic radiation has provided significant insights into the role of cracks in moisture flow in cracked material. However, these imaging methods are often impractical because they are generally limited to small geometries (on the order of a few centimeters), have very high energy demands, require large facilities (such as a nuclear reactor in the case of neutron imaging), may be invasive, and are often expensive to perform [14, 15].

On the other hand, electrically-based methods generally do not have such testing limitations. In particular, Electrical Impedance Spectroscopy (EIS) has been previously used to monitor unsaturated moisture flow in cement-based materials. In the majority of previous research studies utilizing EIS, electrode pairs were embedded in cement-based material, and pairwise impedance measurements between electrodes were performed. For example, McCarter and coauthors [16, 17, 18, 19] embedded electrodes at different vertical depths to detect the depth of the moisture ingress. In the approach proposed by McCarter et al. [19], the maximum rate of impedance change (as a function of time) was assumed to indicate the arrival of the water front at the height of an electrode pair. In addition, Rajabipour et al. [20] developed an analytical function using finite element simulations to relate pairwise impedance measurements to the location of "moisture front." However, the localization of the water front based on the pairwise impedance measurements is possible only if the water front is approximately horizontally aligned, i.e., the water flow is one-dimensional (1D). If the moisture content varies in three dimensions, interpretation of pairwise EIS measurements is a challenging task.

In contrast to EIS, Electrical Resistance Tomography (ERT) reconstructs the spatial distribution of the internal electrical conductivity resulting from moisture ingress without the need of *ad hoc* experimental and/or analytical calibrations. Research reported in [21, 22, 23] was perhaps the first attempt to monitor 2D moisture flow in cement-based material using ERT. More recently, ERT was used to monitor 1D ion and moisture flow in concrete slabs [24]; the ERT reconstructions were corroborated with Ground Penetrating Radar (GPR). In [14] ERT reconstructions of two-dimensional (2D) moisture flow in cement paste were compared with neutron radiography images, showing a good qualitative agreement between the two imaging methods. Further, in [25] ERT was shown to be capable of qualitatively imaging 3D moisture flow in large dimensional objects made of cement-based materials, and in [26], an approach for quantifying the moisture content in cement-based materials using ERT was proposed; the results were in good agreement with simulations of moisture flow.

In all above cited ERT studies, moisture flow was imaged in cement-based materials that were undamaged. The cracking induces an additional difficulty to moisture flow monitoring on the basis of electrical measurements: Cracks are complex 3D structures with high conductivity contrasts – unsaturated cracks being essentially non-conductive inclusions and water-filled cracks being highly conductive. In such conditions, the inference of moisture distibution would be virtually impossible with EIS. ERT, on the other hand, carries more information on the 3D distribution of the electrical conductivity than EIS, and furthermore, previous research has demonstrated the potential of ERT for localizing non-conductive cracks in cement-based materials [27, 28]. However, due to the diffusive nature of ERT, its spatial resolution is usually low [29], and it has a limited ability to simultaneously image inclusions that feature different electrical properties. Hence, the capability to separately detect unsaturated cracks in a uniform background and moisture flow in uncracked material does not guarantee the ability to monitor moisture flow in cracked materials. Therefore, this paper seeks for an answer to the question: Can ERT be used for monitoring 3D unsaturated moisture flow in cement-based materials with discrete cracks?

To address the above question, a series of experiments is carried out, with physically-simulated cracks and with discrete cracks that are generated by split-tensile loading. The physically-simulated cracks have known geometries, which enables a comparison between ERT images and results of moisture flow simulations. Because the specimens used in the experiments are large, neutron and X-ray tomography are not suitable methods for corroboration [25, 26, 30, 8]; thus, the ERT reconstructions of samples with split-tensile loading induced cracks are evaluated only by visual comparison with the photographs of the specimen.

In the following sections, material and sample preparation are discussed, a brief review of the ERT scheme is provided, a method of simulating unsaturated moisture flow is presented, and finally results are reported and discussed.

2. Materials and sample preparation

2.1. General

For determining the feasibility of ERT for monitoring moisture flow in cracked cement-based material, a total of five specimens were prepared. Two specimens had physically-simulated cracks and three had loading-induced discrete cracks. The physically-simulated cracks included a cylindrical through-crack penetrating the entire height of the specimen and a plate-like crack penetrating 2/3 of the specimen height; these specimens are shown in Figures 1a and 1b, respectively. The three specimens with discrete cracks were damaged using split-tension loading and are shown in Figure 2. Two of these specimens had non-metallic fibers to reduce the crack widths and decrease the rate of water ingress. The remaining specimen did not include fibers.

2.2. Materials

All of the specimens were made of ordinary Portland cement (Type I) and fine aggregate (natural river sand, fineness modulus = 2.63). The water-to-cement ratio (w/c) was 0.60 and the volumetric aggregate content was 40.0%. It should be noted that in selecting this mortar mixture, we ignored the contribution of the Interfacial Transition Zone (ITZ). Percolation of ITZ, which may happen at a higher aggregate volume fractions, may enhance the transport properties [31]. The low aggregate content and high water-to-cement ratio was used to increase the capillary porosity of the mortar, thereby increasing the rate of capillary transport in the material. This effectively decreased the experimentation time, which would be longer using a mortar mixture with a higher aggregate content and a lower w/c ratio. While all specimens used the same cement and aggregates, two of the specimens were cast with 0.2% (by volume) non-conductive nylon fiber reinforcement (directly replaced aggregate volume, to ensure identical cement paste content in all specimens) to reduce crack widths resulting from split-tension loading. The nylon fibers were 1.9 cm long (aspect ratio of 70) and had a tensile strength of 966 MPa. The mixing was carried out according to ASTM C192-06 [32].

To create the physically-simulated cracks (shown in Figures 1a and 1b), inclusions were inserted in two of the 10.20 × 20.30 cm cylindrical specimens immediately after casting. To construct the specimen with the cylindrical through-crack, a rod (diameter 1.0 cm) was inserted through the top of the mold lid. The rod, and the induced cylindrical crack, penetrated from top to bottom of the specimen. For the specimen with the plate-like crack, a PVC plate inclusion of dimensions 0.8 cm × 6.6 cm × 6.6 cm was inserted into top of the specimen. After 4 hours, the inserts were removed from the specimens and the specimen molds were completely resealed using new plastic lids. The cylinders were then demolded after 24 hours and cut in half using a wet saw to create the specimens used in ERT tests. In the case of the specimen with the cylindrical through-crack, the bottom of the specimen was secured to a PVC plate using silicon caulking to ensure that the bottom of the specimen was water-tight.

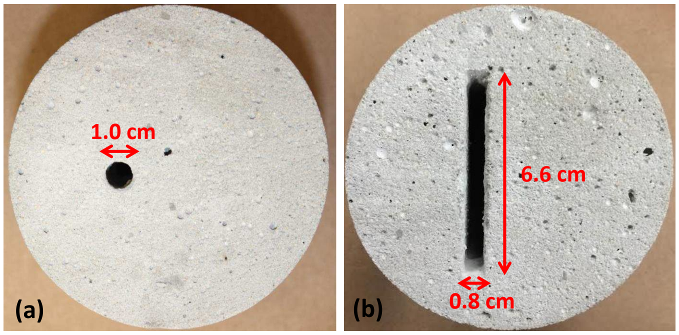

Figure 1: Specimens with physically-simulated cracks; (a) specimen with cylindrical through-crack and (b) specimen with plate-like crack.

.

Due to the high w/c ratio, specimens were saturated after demolding at 24 hours. The specimens were moved to an oven at 50°C for 5 hours to reduce their moisture content. The specimens were then sealed in two layers of plastic bags and placed inside an environmental chamber at 23°C for at least 30 days to achieve uniformity in the distribution of moisture content. The resultant volumetric moisture was determined to be

$\theta_\mathrm{i} = 0.07$ by drying a set of identically-conditioned specimens of the same material and geometry. It should be noted that θ_i was determined from specimens that did not include cracks. However, it can be safely assumed that θ_i was 0.07 also in the specimens with physically-simulated cracks.

After conditioning, the specimens without physically simulated cracks were damaged using the split-tension loading similar to ASTM C496 [33]. In this procedure, each cylindrical mortar specimen was loaded along the length of the specimen with a diametral compressive force. Such a load induces tensile stresses and therefore splitting along the loading plane. Displacement-controlled loading at 0.05 cm/min was used to generate cracks in these specimens.

Since the discrete cracks were difficult to observe in photographs due to the narrow crack widths, the photographs of the specimens were converted to grey scale and then binary images (Figure 2 using image analysis software [34]. In the image analysis, the thresholding method with an arbitrary threshold value (clip level) was used to convert the images from grey scale to binary [35]. This, overall, resulted in overestimation of the actual crack width, which was a function of the clip level. The purpose of Figure 2 is only to provide a visualization of cracks and their locations and to qualitatively illustrate the differences between the crack widths.

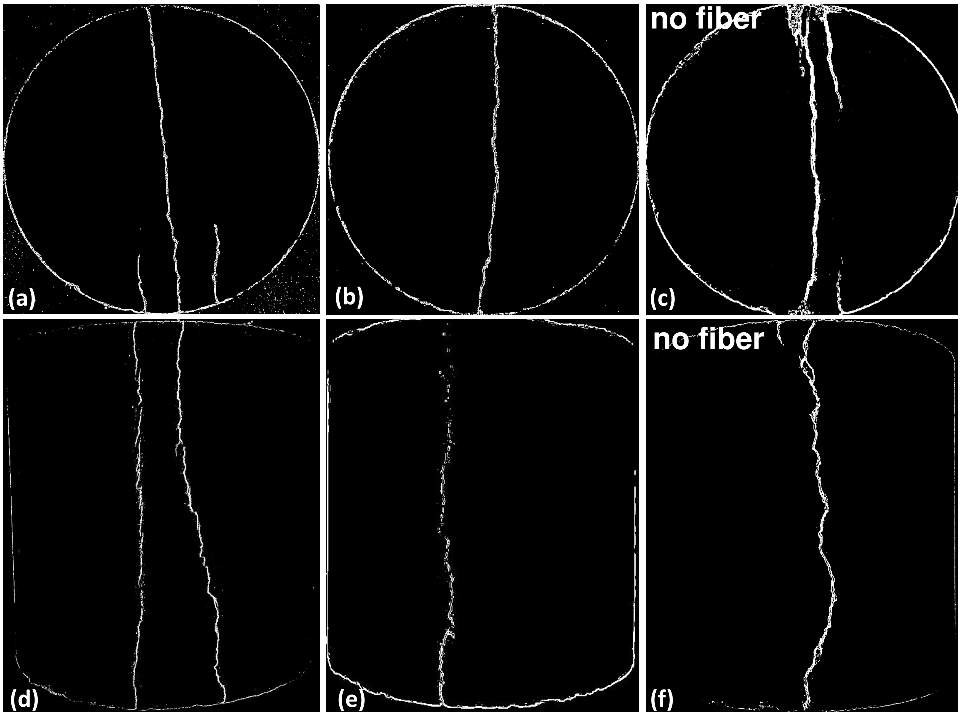

Figure 2: Binary images of specimens with discrete cracks; (a - c) top view of cracked specimens and (d - f) side view of cracked specimens.

.

2.3. Preparation of the ERT samples and water reservoirs

The electrodes used in this work were made of colloidal silver paint which was applied to the surface of the specimen using a small brush. The colloidal silver paint has a low resistivity and is fast drying, making it a suitable material for "painted" electrodes [1, 36]. A total of 24 square electrodes (with dimension of 1.30 cm × 1.30 cm) were painted on the outer surface of the cylindrical specimens. The electrodes were arranged in three equally spaced 8-electrode rings. Figure 3a shows one of the specimens and the locations of the electrodes. After the silver paint electrodes had dried, a 14-gage wire was connected on the surface of each electrode using electric tape. Finally, the connection between electrodes and wires was force-secured using zip-ties.

For specimens with physically-simulated cracks, custom water reservoirs matching the shape of physically-simulated cracks were made from PVC. For specimens with discrete cracks, circular cylindrical PVC pipe water reservoirs were used; they were placed 2.0 cm off center to induce asymmetric water flow in the cracks. The reservoirs had a height of 5.0 cm and an internal diameter of 1.8 cm. A fully-prepared ERT specimen is shown in Figure 3b.

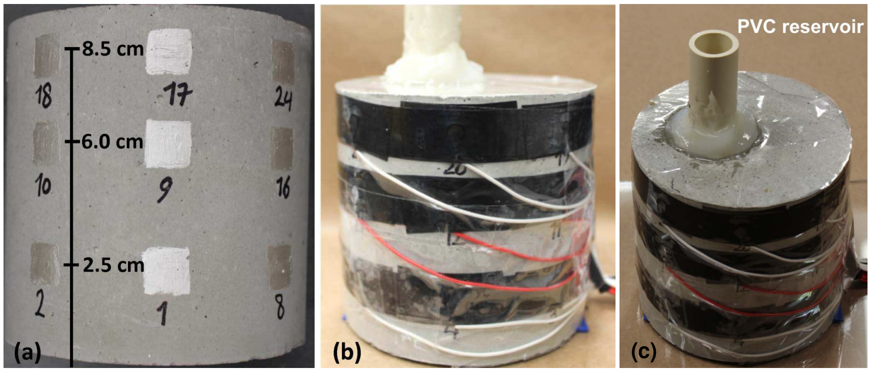

Figure 3: Example of a specimen used in ERT testing: (a) location of the electrodes, (b) fully-prepared ERT specimen, and (c) isometric view including the water reservoir.

.

3. Methods

3.1. Electrical resistance tomography

In Electrical Resistance Tomography (ERT), a set of electrodes is installed on the surface of an object. Electric currents are applied between electrode pairs and resulting potential differences (voltages) are measured between multiple pairs of electrodes. Based on these voltage measurements, the distribution of the electrical conductivity in the object is reconstructed. ERT is a special case of Electrical Impedance Tomography (EIT), an imaging modality which uses both the electrode potential amplitudes and phase shifts between the sinusoidal potentials and the injected currents to reconstruct the electrical admittivity distribution; in ERT, the capacitive effects are neglected [37].

Mathematically, the reconstruction problem in ERT is a non-linear ill-posed inverse problem in the sense that it may not yield stable or unique solutions and generally requires some sort of regularization. A variety of ERT reconstruction methods have been developed [38]. Broadly, *difference imaging* and *absolute imaging* are the most commonly used schemes. In difference imaging, the change in electrical conductivity is reconstructed from potential measurements corresponding to two states. One advantage of difference imaging is its robustness to modeling and systematic measurement errors, because the errors partially cancel due to subtraction of the two data sets. Difference imaging, however, is often *qualitative* and has a very low resolution due to the linearization of the nonlinear estimation problem [39]. In contrast to difference imaging, absolute imaging *quantitatively* reconstructs conductivity by solving the full non-linear ERT problem.

In this work, the ERT reconstructions were computed within the absolute imaging framework. However, because the target of primary interest in this work was the moisture content, the crack pattern within the specimen was considered as an auxiliary unknown, which was not explicitly modeled/estimated – instead, the initial conductivity was modeled as homogeneous, and the inhomogeneity related to cracking was accounted for only via introducing an approximative modeling error term which was calculated based on reference ERT measurements of the cracked specimens before the water ingress. This approach, adopted from [40], circumvents the drawbacks of the standard reconstruction methods, namely: 1) errors caused by linearization of the highly non-linear model in standard difference imaging, and 2) the difficulty of the standard absolute reconstruction problem, associated with the high complexity of the conductivity distribution in the presence of both unsaturated and saturated cracks. For an alternative, non-linear difference imaging -based approach to account for the inhomogeneity of the background conductivity, see [41].

To solve the inverse problem of ERT, a forward model is needed. The most accurate forward model for the ERT measurements, known to date, is the Complete Electrode Model [42, 43]. The CEM consists of the partial differential equation

$$\nabla \cdot (\sigma \nabla u) = 0, \quad x \in \Omega \tag{1}$$

and the boundary conditions

$$u + \xi_l \sigma \frac{du}{d\bar{n}} = U_l, \quad x \in e_\ell,\ \ell = 1, \ldots, L \tag{2}$$

$$\sigma \frac{du}{d\bar{n}} = 0, \quad x \in \partial\Omega \backslash \bigcup_{\ell=1}^{L} e_\ell \tag{3}$$

$$\int_{e_l} \sigma \frac{du}{d\bar{n}}\, dS \ = I_l, \quad \ell = 1, \ldots, L \tag{4}$$

where Ω is the target volume, and $\partial\Omega$ is its boundary, σ is the electrical conductivity, u is the electric potential, $\bar{n}$ is the outward unit normal, e_l is the l^{th} electrode, and ξ_l, U_l and I_l, respectively, are the contact impedance, electric potential and total current corresponding to e_l. Moreover, the current conservation law must be fulfilled

$$\sum_{l=1}^{L} I_l = 0 \tag{5}$$

and the potential reference level must be fixed, for example by writing

$$\sum_{l=1}^{L} U_l = 0. \tag{6}$$

To approximate the solution of the CEM (Eqs. (1 - 6)) for an object of arbitrary geometry we used the Finite Element Method (FEM) [44, 45]. Assuming a Gaussian noise model, the observation model for the ERT measurements gets the form

$$V = U(\sigma) + e \tag{7}$$

where V is a vector consisting of the measured electrode potentials, $U(\sigma)$ is the finite element (FE) -based approximation for the mapping between a discretized conductivity distribution σ and electrode potentials V, and e is the Gaussian-distributed noise. For details of the forward model, we refer to [45].

Reconstructing σ from potential measurements V is an ill-posed inverse problem. This means that classical solutions, such as least-squares estimate for σ, are practically always non-unique and extremely intolerant to measurement noise and modeling errors [46]. Due to the ill-posedness, we employed so-called Tikhonov regularization [44], and estimated σ as a solution of the following constrained minimization problem

$$\widehat{\sigma} = \arg\min_{\sigma > 0} \left[\| L_{\mathrm{e}} (V - U(\sigma) - \epsilon) \|^2 + p(\sigma) \right] \tag{8}$$

where L_{e} is the Cholesky factor of the noise precision matrix and $p(\sigma)$ is a regularizing function (see below). Further, ϵ is an approximative modeling error term defined by

$$\epsilon = V_{\mathrm{ref}} - U(\sigma_{\mathrm{ref}}) \tag{9}$$

where V_{ref} is a vector consisting of the ERT measurements at the reference state (i.e., before introducing water) and $U(\sigma_{\mathrm{ref}})$ is a vector of computed potentials corresponding to σ_{ref}, a homogeneous estimate for the of non-homogeneous conductivity of a specimen at the reference state. Here, the homogeneous estimate was chosen to be $\sigma_{\mathrm{ref}} = 0.28$ (mS/cm), the electrical conductivity resulting from the sample conditioning described in Section 2.2. Thus, the error term ϵ accounted for the discrepancy in the electric voltages resulting from the presence of the cracks and the non-uniformity of the initial moisture content distribution. For further discussion of the error model, see [40].

The regularization function, $p(\sigma)$, carries prior information on the conductivity, and is generally formulated such that it penalizes for undesirable or improbable features of σ. Therefore, $p(\sigma)$ has a significant influence on the solution of the inverse problem [47, 48, 49]. In this work, smoothness-promoting regularization [50] was used, as it is particularly applicable to diffusive processes, such as moisture flow in porous media. In smoothness-promoting regularization, the regularizing function takes the form $p(\sigma) = \alpha\|L_\sigma\|^2$, where L_σ is a spatially weighted discrete differential operator and α is a parameter which controls the weight of the side constraint in the solution [46, 51]. Finally, in the solution (8), the constraint $\sigma > 0$ was written based on the physical constraint that electrical conductivity is always positive.

It should be noted herein that in cases of physically-simulated cracks that were large and had known geometries, it would have been possible to model cracks as boundaries in the FE model [52], similarly to models used for moisture flow simulations in next section. However, in the specimens featuring load-induced cracks – as well as in the potential applications of the method – the crack shapes are not known. For this reason, the cracks boundaries were not modeled in any of the the FE geometries.

To reconstruct the discretized conductivity distribution σ by solving the constrained optimization problem (9), the Gauss-Newton method was used. The forward model was solved using tetrahedron elements with a maximum dimension of 2.0 mm, resulting in 828,188 elements. The mesh size was selected based on separate grid coarsening studies; the chosen grid was found to ensure sufficient accuracy of the ERT forward model while maintaining a feasible computational expense. The accuracy of the forward model affects the resolution of ERT reconstructions. It should be noted, however, that the resolution is also affected by various other factors, e.g., placement of the electrodes, measurement noise level, and the regularization methods used in the image reconstruction. Generally, the resolution of ERT is relatively low, due to the ill-posedness of the associated inverse problem [46].

The ERT forward model geometries were modeled as solid cylinders. All ERT calculations were carried out using MATLAB and an adaptation of [53, 54] coupled with parallel processes on 12 quad-core processors using 48 Gb of total memory and implementation of [55] to solve the systems of linear equations.

3.2. ERT measurement strategy

The ERT measurements were carried out using an in-house developed ERT equipment described in [14]. In all measurements, an alternating current with 0.10 mA amplitude and 40 kHz frequency was used. This frequency was chosen based on Electrical Impedance Spectroscopy (EIS) measurements; at frequency 40 kHz, the imaginary component of the impedance was at the minimum. We note herein that the selected frequency based on the EIS measurements, applies only the material tested in this work since the frequency at which the imaginary component of the impedance is minimum (the cutoff frequency) changes depending on the microstructure of the material [56, 57]. One of the factors affecting the cutoff frequency is the moisture content. The moisture content changes, of course, during an ingress experiment and may affect the cutoff frequency. Therefore, the chosen cutoff frequency based on the initial condition of the material (40 kHz here) may not be the most appropriate frequency during the entire duration of the experiment. Further investigation on the effect of varying the measurement frequency during the experiment is required to fully realize the effect of cutoff frequency on the ERT reconstructions.

The accuracy of the potential measurements was $\pm 1.0 \times 10^{-8}$ V. In the ERT measurements, current was injected between electrodes i and j where $i, j = \{1, ..., 24\}$ and $i \neq j$. Corresponding to each current injection, potential measurements were taken with respect to a common ground. A total of 561 current injections and 4488 potential measurements were taken for each set of ERT measurements.

3.3. Numerical simulation of unsaturated moisture flow

3.3.1. Richards' Equation

Isothermal unsaturated moisture flow in porous media was simulated using Richards' Equation [58, 59]:

$$\frac{\partial\theta}{\partial t} = \frac{\partial}{\partial x}\left(K(h)\frac{\partial h}{\partial x}\right) + \frac{\partial}{\partial y}\left(K(h)\frac{\partial h}{\partial y}\right) + \frac{\partial}{\partial z}\left(K(h)\frac{\partial h}{\partial z} + 1\right) \tag{10}$$

where $K = K(h)$ (mm/hour) is the unsaturated hydraulic conductivity, θ (mm^3/mm^3) is the volumetric moisture content, h (mm) is the pressure head, and x, y, and z (mm) are spatial coordinates. As described in [60], air voids affect the transport properties of cement-based materials. In Equation (10), however, air diffusion and dissolution are neglected and only capillary suction is simulated. We note that air diffusion and dissolution occur primarily in late stages of moisture ingress [61, 62, 2], while capillary suction is the main governing transport mechanism at early stages of unsaturated moisture ingress [63]. Since this work considers moisture transport for durations less than 24 hours, neglecting the effects of air diffusion and dissolution can be considered an appropriate approximation.

3.3.2. Material model

Commonly, the unsaturated hydraulic conductivity is expressed as the product of the relative hydraulic conductivity, K_r, and the saturated hydraulic conductivity, K_s, such that $K = K_\mathrm{r}K_\mathrm{s}$. Here, K_s was measured experimentally as described in Section 3.3.3. For unsaturated porous media, Mualem's equation [64] is used to describe K_r:

$$K_\mathrm{r} = \Theta^I \left[\frac{\int_0^{\Theta} \frac{1}{h(x)}, dx}{\int_0^{1} \frac{1}{h(x)}, dx} \right]^2 \tag{11}$$

$$\Theta = \frac{\theta - \theta_\mathrm{r}}{\theta_\mathrm{s} - \theta_\mathrm{r}} \tag{12}$$

where $0 \leq \Theta \leq 1.0$ is the effective material saturation and θ_r is the residual moisture content. $\theta_\mathrm{r} = 0$ is generally considered as an appropriate assumption for cement-based materials [65, 8]. θ_s is the saturated moisture content that was measured experimentally. I is the tortuosity and pore connectivity parameter and in this work $I = -9.0$ was taken from [66]. In [66], I was determined by fitting the results of numerical simulations to the experimentally obtained sorptivity data using the maximum likelihood least squares fitting approach. While the parameter I has been described as the tortuosity and pore-connectivity parameter, in [64], this parameter is not, strictly speaking, a descriptor of classical tortuosity [67, 4] or pore connectivity [68]. Indeed, in works such as [69] and [70], it was argued that I is fitting parameter with no physical meaning. Further discussion of I in cement-based materials is provided in [71] and [70].

In order to calculate the integrals in Eq. (11), the effective material saturation was expressed as a function of the pressure head, $\Theta = \Theta(h)$. We used the van Genuchten model [72, 73], which is of the form

$$\Theta = \frac{1}{[1 + (\alpha h)^n]^m}, m = 1 - \frac{1}{n} \tag{13}$$

where α (mm^{-1}) and $n(-)$ are fitting parameters. For other models, see [74, 69]. For cement-based materials, instead of expressing water retention as $\Theta = \Theta(h)$, the material sorption isotherm is generally obtained experimentally as $\Theta = \Theta(RH)$, where RH denotes relative humidity. It should be noted that this work neglected hysteresis effect for simplicity. As mentioned by [75, 76] and [77] rewetting decreases the unsaturated and saturated hydraulic conductivities. This would imply that our model overestimated unsaturated hydraulic conductivity since we did not account for rewetting. Therefore, without knowing the rewetting isotherm there is some uncertainty regarding the extent to which the unsaturated hydraulic conductivity was decreased. To convert the experimentally obtained isotherm $\Theta(RH)$ to the moisture retention curve as $\Theta(h)$, the Kelvin-Laplace Equation was used [8][78]:

$$h = \frac{\rho_\mathrm{w} RT}{m_\mathrm{w}} \ln(RH) \tag{14}$$

where ρ_w (kg/m^3) is the density of water, $R = 8.845$ JK^{-1}mol^{-1} is the universal gas constant, and m_w (kg/mol) is the molecular weight of water. By fitting the model (13) to the water retention curve $\Theta(h)$, van Genuchten parameters $\alpha = 2.63 \times 10^{-2}$ (mm^{-1}) and $n = 1.77$ were obtained. Figure 4 shows the fitted van Genuchten model and experimentally obtained data points.

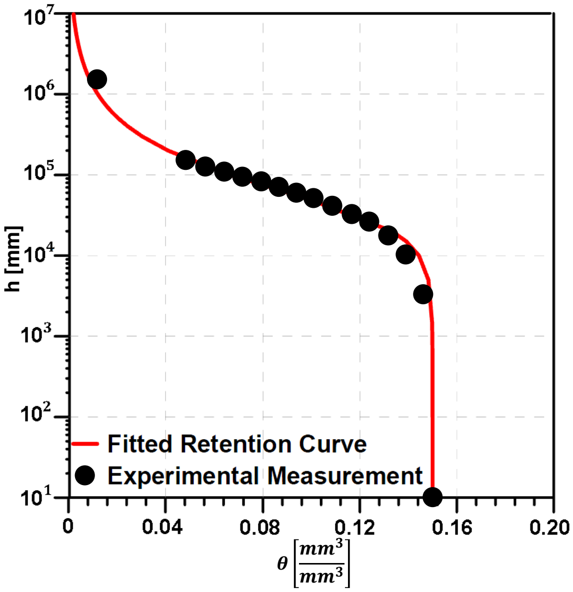

Figure 4: Moisture retention curve for mortar using van Genuchten fitting

3.3.3. Determination of moisture transport model parameters

In this work, moisture flow simulations were only used to corroborate ERT reconstructions, and as such, simulation of moisture flow was not the main objective of this paper. We, therefore, only provide a brief description of the methods to obtain transport modeling parameters. Complete details of methods to simulate moisture flow can be found in [79, 66, 61, 80, 65, 8].

The saturated hydraulic conductivity K_s was determined using an in-house developed equipment and the application of Darcy's law following procedures in [3], yielding $K_\mathrm{s} = 5.0 \times 10^{-3}$ (mm/hr). The saturated moisture content θ_s was determined from drying initially saturated specimens at 105°C for 48 hours, resulting $\theta_s = 0.15$. We note that by drying at 105°C for 48 hours, θ_s may be overestimated due to the potential dehydration of ettringite and other phases within the cement paste as well as the release of physically adsorbed water on the C-S-H gel. Further, the initial moisture content θ_i was calculated using the drying procedure detailed in Section 2.2, and was determined to be $\theta_\mathrm{i} = 0.07$. Finally, the desorption isotherm was experimentally measured using an automated sorption analyzer [80, 65]. A summary of the experimentally obtained parameters (K_s, θ_i, and θ_s) and van Genuchten modeling parameters (α, n, I, and θ_r) are provided in Table 1. The parameters shown in Table 1 were used in all simulations.

Table 1: Moisture flow simulation hydraulic parameters

K_s $(\frac{\mathrm{mm}}{\mathrm{hr}})$	θ_s $(\frac{\mathrm{mm}^3}{\mathrm{mm}^3})$	θ_i $(\frac{\mathrm{mm}^3}{\mathrm{mm}^3})$	θ_r $(\frac{\mathrm{mm}^3}{\mathrm{mm}^3})$	I $(-)$	α $(\frac{1}{\mathrm{mm}})$	n $(-)$
0.005	0.15	0.07	0	-9.0	0.026	1.77

3.3.4. Simulation of moisture flow in specimens with physically-simulated cracks

Commercially available Finite Element Software HYDRUS 3D [81] was used to simulate unsaturated moisture flow in specimens with physically-simulated cracks. Zero-flux boundary conditions were applied to all surfaces except the surfaces from which water penetrated. For both specimens, a Dirichlet boundary condition $\Theta = 1.0$ was written for the outer surface of the crack, i.e., the material in contact with water was modeled as fully saturated. The uniform initial moisture content $\theta_\mathrm{i} = 0.07$ was considered, as discussed in Section 2. The model geometries are shown in Figure 5. The finite element mesh consisted of tetrahedral elements with a maximum dimension of 2 mm. The finite element model was solved in terms of moisture content.

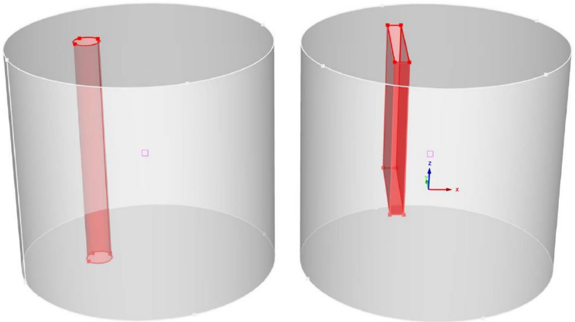

Figure 5: Boundary conditions used in simulations of unsaturated moisture flow in specimens with artificial cracks; saturated boundary conditions (red, crack surfaces) and zero-flux boundary conditions (gray, on all other surfaces)

4. Results and discussion

4.1. ERT reconstructions of moisture flow in physically-simulated cracks

Figure 6 shows the results of the experiments and moisture flow simulations for specimens with physically-simulated cracks. Figure 6a corresponds to the specimen with the cylindrical physically-simulated through-crack, and Figure 6b to the plate-like crack. Both in Figure 6a and 6b, the first row represents the ERT-based reconstructions of the conductivity distribution σ after 1, 4, 12, and 24 hours of moisture ingress, and the second row shows the simulated water content θ at the respective times. Note that the images representing θ show the water content within the computational domain, which excludes the contents of the cracks (cf. Fig. 5) – within the water-filled cracks, the water content is naturally equal to 1. Note also that the conductivity of the unsaturated mortar (0.95) is assigned as transparent in the images representing the conductivity distributions; this enables the visualization of the volumes of higher conductivity in 3D. The far left column in the figure shows top view of the specimens.

The ERT-reconstruction corresponding to time of 1 h water ingress in the specimen with cylindrical through-crack features a high conductivity in a volume, the shape and size of which are very similar to the crack; that is, ERT has successfully located the cylindrical crack in the saturated condition. The conductivity outside the crack is almost uniform and lower than within the crack, suggesting that water has not yet absorbed significantly to the surrounding material. The simulated water content θ at time 1 h is in agreement with this result, θ being above the initial moisture content (0.07) only in the close neighborhood of the cylindrical crack. In the subsequent time steps (4, 12 and 24 h), the volume with high conductivity increases steadily. The reconstructed conductivity distributions are again in a very good agreement with the moisture flow simulation, featuring mutually very similar shape in the volumes of high σ and θ. The series of images in Figure 6a suggest that ERT is able to capture the ingress of water in the surrounding material.

In the second experiment (Figure 6b), the plate-like crack is localized by ERT. The vertical dimension of the crack (2/3 of the specimen height) is traced relatively well, while tracing the length of the crack in horizontal direction is less successful. As noted above, ERT is generally an imaging modality with a relatively low resolution. Moreover, the resolution of ERT is generally not uniform within an object; the spatially dependent resolution is affected, e.g., by the geometry of the object, placement of the electrodes, and the regularization as well as other computational methods used in the image reconstruction [82]. Nevertheless, the series of images corresponding to times 1, 4, 12 and 24 h shows the penetration of water to the material around the crack. Again, the ERT reconstructions correspond to the results of moisture flow simulation relatively well, supporting the ability of ERT to image water flow in cracked cement-based material.

We emphasize that the above comparison between the results of ERT and moisture flow simulation is only qualitative, because ERT reconstructions report electrical conductivity σ (mS/cm), whereas simulations of moisture flow report the volumetric moisture content θ (mm^3/mm^3). Note that the relationship between σ and θ is nonlinear [26].

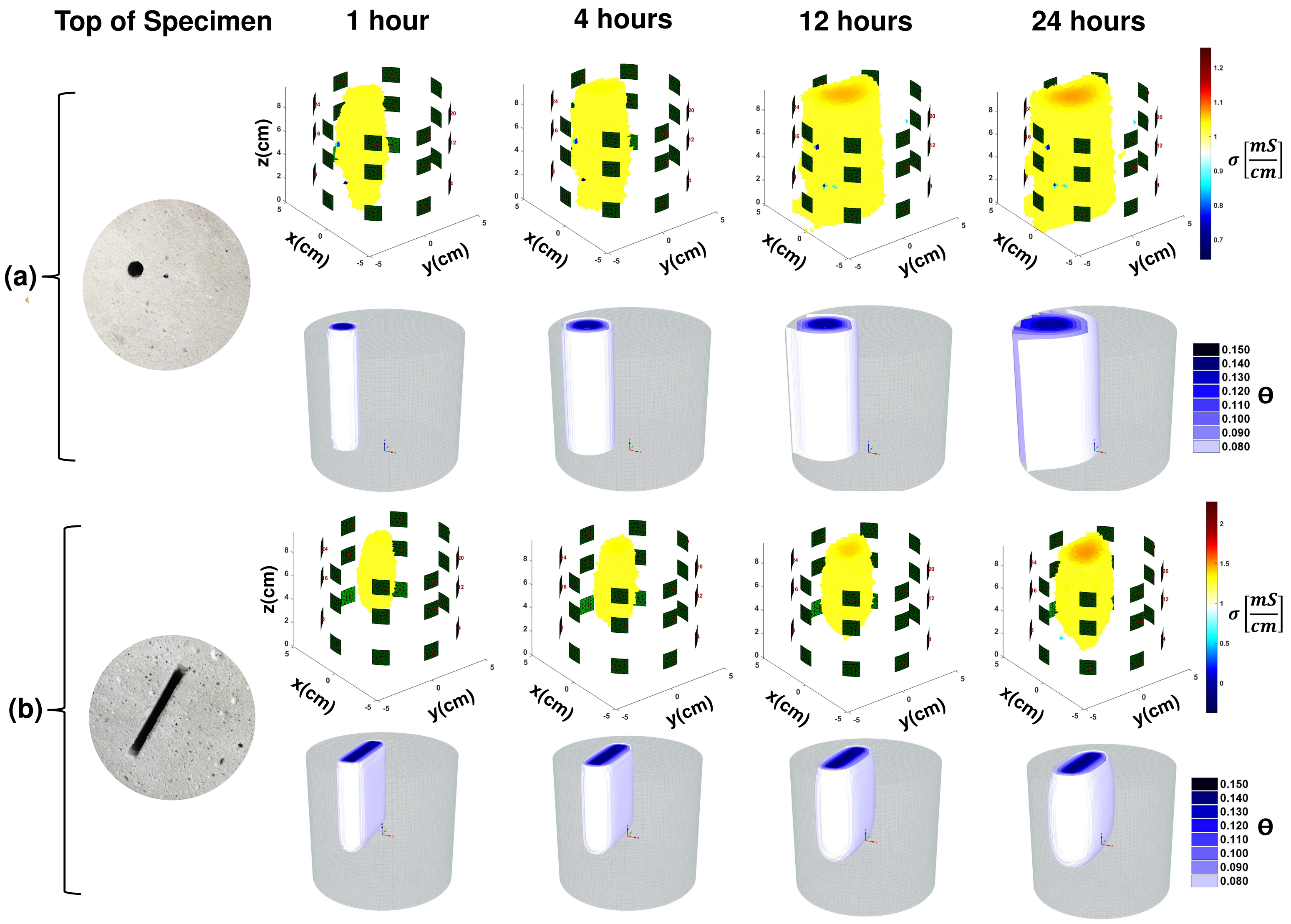

Figure 6: 3D ERT reconstructions of the electrical conductivity σ and simulated water content θ corresponding to 1, 4, 12, and 24 hours of ingress in: (a) mortar specimen with the physically simulated cylindrical through-crack, and (b) mortar specimen with the plate-like crack. Top view of each specimen is shown in the far left column.

4.2. ERT reconstructions of moisture flow in load-induced cracks

ERT reconstructions of the three specimens with loading-induced discrete cracks are visualized in Figures 7 and 8. While Figure 7 illustrates the reconstructed conductivity distributions as 3D contour plots, Figure 8 represents the conductivities on 2D horizontal slices at heights of 2, 4.5, 7, and 9.5 cm from the bottom of the specimens. In both figures, the results of the two fiber reinforced specimens are shown in the first two lines, and the results of the mortar specimen without fiber reinforcement in the third line. Again, in Figures 7 and 8, the conductivity of the unsaturated mortar (0.95) is assigned as transparent, to enable the visualization of the volumes of higher conductivity in 3D. The far left columns show the binary images of the top of the specimens.

For the first fiber reinforced specimen (Figures 7a and 8a), the ERT reconstruction corresponding to 15 min of water ingress shows increase of conductivity directly under the water reservoir and in a volume extending from the location of the reservoir towards the side surface of the cylindrical specimen – i.e., to the direction of the visible crack under the reservoir (cf. the binary image in Figure 7a, left). In the subsequent times (1, 4, 12 and 24 h), the volume of the high conductivity continues to extend, both horizontally and vertically. The increase of conductivity is clearly strongest along the crack (see especially Figure 8a). The reconstructed evolution of the conductivity has features that were expected for the ingress of moisture in a cracked fiber-reinforced specimen: a crack saturates when in contact with water, and acts as a source of water ingress for the surrounding material, similarly to the simple cases of physically simulated cracks in Figure 6. Here, however, the ERT images indicate that in the beginning of the experiment, only a portion of the crack gets saturated – north west direction from the reservoir, and not very deep vertically, yet the crack extends horizontally through the entire diameter and vertically through the entire height of the specimen (cf. Figure 2). This is also a plausible result, because the fiber reinforcement keeps portion of the cracks in the specimen narrow, and the narrowest parts of the cracks do not saturate as quickly as the wide part of the crack. Indeed, the volumetric flow rate in a parallel-plate crack (Q_c) has been shown to increase proportionally to the cubic power of crack width (w_c) [3], i.e $Q_\mathrm{c} \propto w_\mathrm{c}^3$. The observation of the conductivity increase being strongest along the crack over the time-series was also an expected result: It indicates that the crack offers a preferred pathway for the moisture ingress over the surrounding porous material.

In the case of the second fiber reinforced specimen (Figures 7b and 8b), the conductivity again increases quickly in the location of the crack under the reservoir (cf. the binary image in Figure 7b, left). Here, the region of increased conductivity covers the entire length of the crack in the horizontal direction already in the reconstruction corresponding to 15 min of water ingress. Vertically, however, the region of increased conductivity only about 1/3 of the specimen height, which is probably again due to a narrow crack width caused by the fiber reinforcement. However, the images of the reconstructed conductivity at times 1, 4, 12 and 24 h of water ingress show that the conductivity increases most strongly in the direction along the crack. Simultaneously, the volume of the increased conductivity spreads in all other directions, again indicating the capability of ERT to image the ingress of moisture in the material surrounding the crack.

In the last specimen (Figures 7c and 8c), the evolution of the conductivity distribution has mostly similar properties to the previous cases: the increase of conductivity along the crack, and spreading of the conductive region caused by the penetration of moisture to the cement-based material. The difference between this case and the previous two cases is that here, the conductivity increases rapidly within the entire extent of the crack under the water reservoir: The region of increased conductivity has already extended to the bottom of the specimen after 15 min of water ingress. This is again an expected result, because this specimen was not reinforced with fibers; it thus featured wider cracks which saturated rapidly.

In summary, the experiments with the specimens with loading-induced discrete cracks resulted ERT reconstructions which clearly illustrate the flow of moisture in a cracked cement-based material. In the absence of a proper corroboration method (such as an alternative imaging modality) for verifying the results, the ERT reconstructions of the specimens with loading-induced discrete cracks were only evaluated based on visual inspection of the crack pattern on the surfaces of the specimens. The reconstructed images are in a good agreement with the visual observation, and they conform well with the known properties of the unsaturated moisture flow in cement-based materials – indeed, the coupled moisture flow in cracks and the surrounding material observed in the ERT reconstructions can be characterized as a well-known mobile-mobile (dual permeability) moisture transport [79, 83, 5]. These results, together with the findings of the experiments reported in Section 4.1, strongly support the feasibility of ERT for imaging unsaturated moisture flow in cement-based materials with discrete cracks.

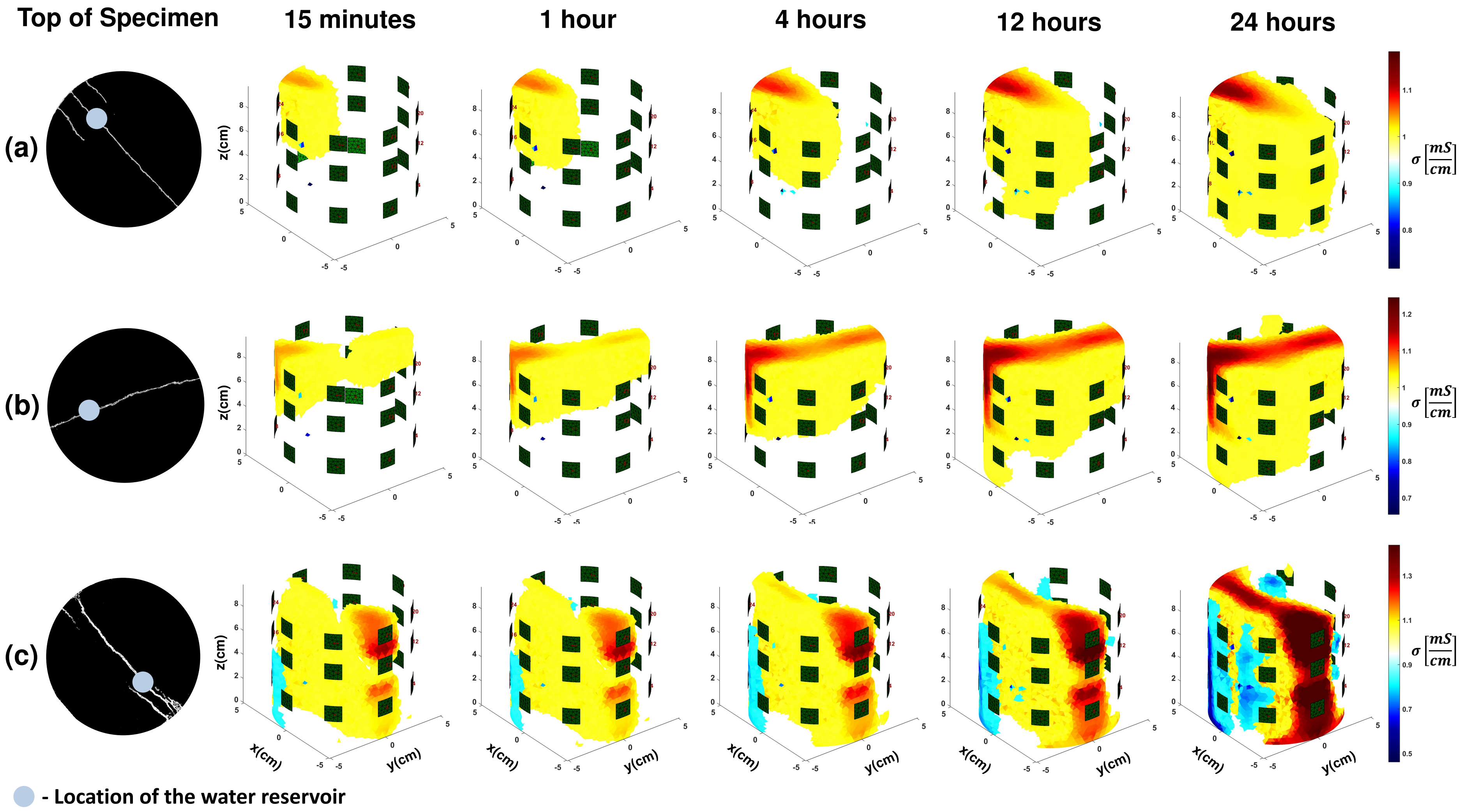

Figure 7: 3D ERT reconstructions of unsaturated moisture flow in discrete cracks for 15 minutes, 1, 4, 12, and 24 hours of ingress in: (a, b) mortar specimens with non-metallic fiber reinforcement and (c) the mortar specimen without fiber reinforcement. The water reservoir location and a binary image of the top of the specimen shown in the far left column.

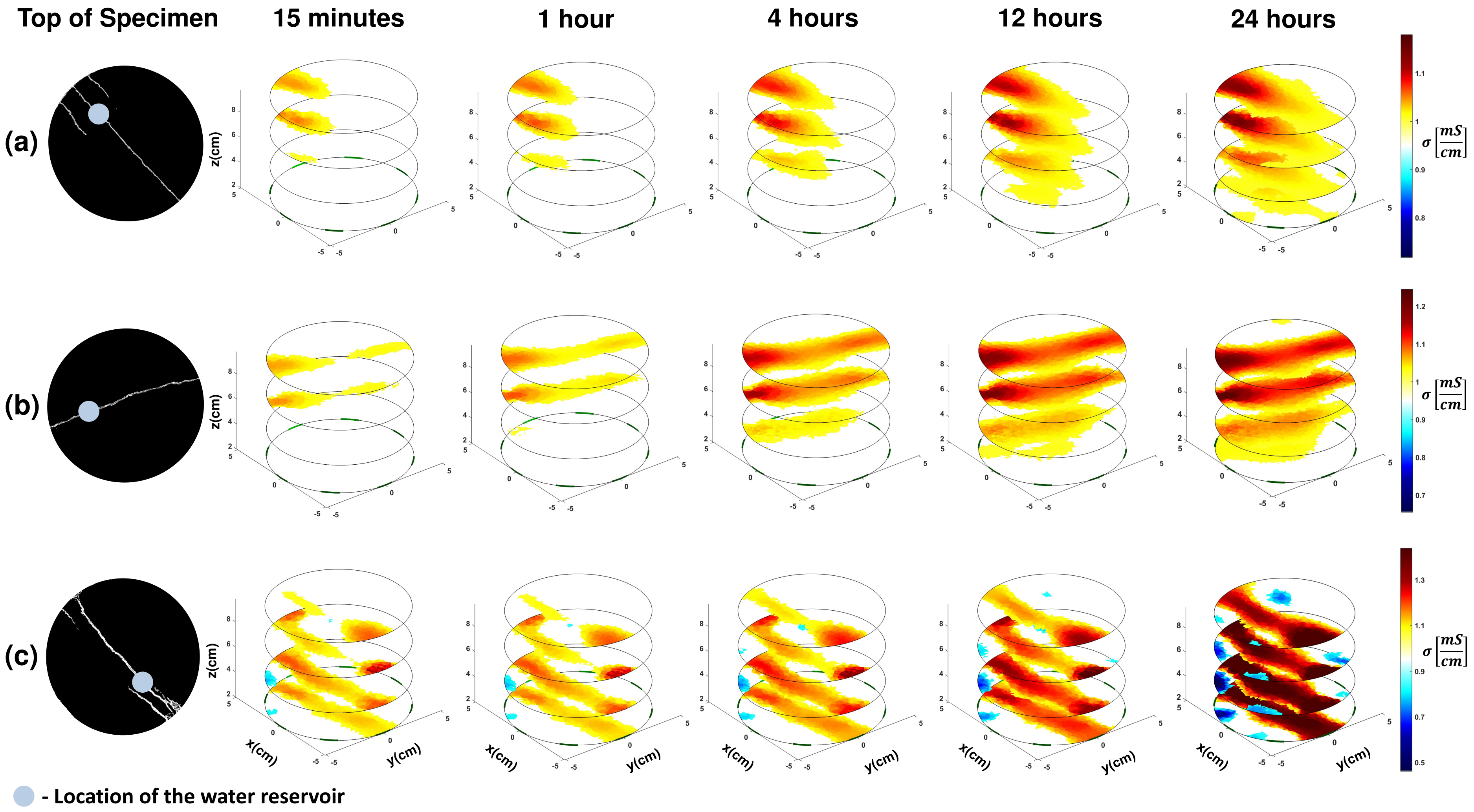

Figure 8: 2D horizontal slices of 3D ERT reconstructions of unsaturated moisture flow in discrete cracks for 15 minutes, 1, 4, 12, and 24 hours of ingress in: (a, b) mortar specimens with non-metallic fiber reinforcement and (c) the mortar specimen without fiber reinforcement. The water reservoir location and a binary image of the top of the specimen shown in the far left column.

5. Summary and conclusions

Cracks provide preferential pathways for moisture to flow into cement-based materials. Cracking therefore significantly reduces material resistance to moisture ingress and, consequently, durability. Yet, few methods offer ample resolution to visualize moisture flow in cracked materials without significant testing constraints. The aim of this paper was to determine if ERT could be used to monitor 3D unsaturated moisture flow in cement-based material with discrete cracks. This topic was studied experimentally. In the first set of experiments, the mortar specimens contained physically-simulated cracks of known geometries, and the ERT reconstructions were compared with numerical simulations of unsaturated moisture flow. Next, mortar specimens with loading-induced cracks were subjected to moisture ingress. Two of these specimens were reinforced with non-metallic fibers, and one specimen was made of plain mortar. These materials were selected to alter the crack widths and permeability of cracks, with the intention to create different flow regimes. In the absence of a proper corroboration method, the ERT reconstructions of the specimens with loading-induced cracks were evaluated qualitatively based on visual observations and known properties of unsaturated moisture flow.

In all specimens, 3D moisture flow in cracks and the surrounding material was captured with ERT. Progressive flow of water in cracks was observed, confirming that ERT can be used to visualize differing rates of water ingress in cracks with dissimilar geometries and permeabilities. The results confirm that ERT is a feasible modality for imaging unsaturated moisture flow in cement-based materials with discrete cracks. The application of ERT to visualize moisture flow in cracks and the surrounding material may be extended to many cracked porous materials and various specimen geometries. In this work a cylindrical geometry was used, therefore, applicability of ERT to visualize features in irregular geometries requires further research. Especially, in the case of large geometries and geometries that constrain physical access for measurement (e.g., frames, beams, foundations, and dams) the use of advanced computational and approximation techniques may be necessary and requires further research.

Acknowledgments

This work was conducted in the Materials and Sensor Development Laboratory (MSDL) and Constructed Facilities Laboratory (CFL) at North Carolina State University (NCSU). The authors would like to acknowledge the CFL laboratory support staff who made this research possible. Computations were carried out using the High-Performance Computing (HPC) Load-Sharing Facility (LSF), a service provided by the NCSU Office of Information Technology (OIT). In addition, the authors acknowledge the expertise from Dr. Gary Howell and Dr. Jianwei Dian for the technical assistance in using the LSF environment. The third author would like to acknowledge the support provided by Academy of Finland (projects 270174 and 273536). This support is greatly acknowledged.

References

[1] M. Pour-Ghaz, Detecting damage in concrete using electrical methods and assessing moisture movement in cracked concrete, Ph.D. thesis, Purdue University, Indiana (2011).

[2] C. Hall, W. Hoff, Water transport in brick, stone and concrete, 2nd Edition, Taylor & Francis, London and New York, 2012.

[3] F. Ghasemzadeh, M. Pour-Ghaz, The effect of damage on moisture transport in concrete, J. Mat. Civil Eng. (2014) DOI: 10.1061/(ASCE)MT.1943–5533.0001211.

[4] A. Akhavan, S. M. Shafaatian, F. Rajabipour, Quantifying the effects of crack width, tortuosity, and roughness on water permeability of cracked mortars, Cem. Concr. Res. 42 (2) (2011) 313–320.

[5] J. Daïan, J. Salbia, Transient moisture transport in a cracked porous medium, Transport Porous Med. 13 (1993) 239–260.

[6] S. Roels, K. Vandersteen, J. Carmeliet, Measuring and simulating moisture uptake in a fractured porous medium, Adv. Water Resour. 26 (3) (2003) 237–246.

[7] S. Roels, J. Carmeliet, Analysis of moisture flow in porous materials using microfocus X-ray radiography, Int. J. Heat Mass Transf. 49 (25-26) (2006) 4762–4772.

[8] M. Pour-Ghaz, F. Rajabipour, J. Couch, J. Weiss, Numerical and experimental assessment of unsaturated fluid transport in saw-cut (notched) concrete elements, ACI Special Publication 266 (2009) 73–86.

[9] M. Pour-Ghaz, F. Rajabipour, J. Couch, J. Weiss, Modeling fluid transport in cementitious systems with crack-like (notch) geometries, International RILEM Workshop on Concrete Durability and Service Life Planning. Haifa, Israel 2009 (2009) 71–79.

[10] M. Kanematsu, I. Maruyama, T. Noguchi, H. Iikura, T. N., Quantification of water penetration into concrete through cracks by neutron radiography, Nucl. Instrum. Methods Phys. Res. Sect. A. 605 (1-2) (2009) 154–158.

[11] J. Carmeliet, J.-F. Delerue, K. Vandersteen, S. Roels, Three-dimensional liquid transport in concrete cracks, International Journal for Numerical and Analytical Methods in Geomechanics 28 (2004) 671–687.

[12] D. Fukuda, Y. Nara, Y. Kobayashi, M. Mauyama, M. Koketsu, D. Hayashi, H. Ogawa, K. Kaneko, Investigation of self-sealing in high-strength and ultra-low-permeability concrete in water using microfocus x-ray ct, Cement and Concrete Res. 42 (2012) 14941500.

[13] W. Li, M. Pour-Ghaz, P. Trtik, M. Wyrzykowski, B. Münch, P. Lura, P. Vontobel, E. Lehmann, W. J. Weiss, Using neutron radiography to assess water absorption in air entrained mortar, Const Build Mater 110 (2016) 98 – 105.

[14] M. Hallaji, A. Seppänen, M. Pour-Ghaz, Electrical resistance tomography to monitor unsaturated moisture flow in cementitious materials, Cement and Concrete Res. 69 (2015) 10–18.

[15] W. McCarter, T. Chrisp, G. Starrs, A. Adamson, E. Owens, P. Basheer, S. Nanukuttan, S. Srinivasan, N. Holmes, Developments in performance monitoring of concrete exposed to extreme environments, J. Infrastruct. Syst. 18 (3) (2012) 167–175.

[16] W. McCarter, D. Watson, Wetting and drying of coverzone concrete, in: Inst. Civ. Eng. Struct. Build., Vol. 112, 1997, pp. 227–236.

[17] W. McCarter, Monitoring the influence of water and ionic ingress on cover zone concrete subjected to repeated absorption, Cement Concrete Aggr. 18 (1) (1996a) 55–63.

[18] W. McCarter, H. Ezirim, M. Emerson, Properties of concrete in the cover zone: Water penetration, sorptivity, and ionic ingress, Mag. Concrete Res. 48 (176) (1996b) 149–156.

[19] W. McCarter, M. Emerson, H. Ezirim, Properties of concrete in the cover zone: Developments in monitoring techniques, Mag. Concrete Res. 47 (172) (1995) 243–251.

[20] F. Rajabipour, J. Weiss, J. Shane, T. Mason, P. Shah, Procedure to interpret electrical conductivity measurements in cover concrete during rewetting, J. Mater. Civil Eng. 17 (5) (2005) 586–594.

[21] W. Daily, A. Ramirez, A. Binley, S. Henry-Poulter, Electrical resistance tomography of concrete structures, in: ECAPT94: 3rd European concerted action meeting on process tomography, Lisbon, Portugal, 1994.

[22] M. Buettner, A. Ramirez, W. Daily, Electrical resistance tomography for imaging concrete structures, in: Structural materials technology an NDT Conference, San Diego, California, 1996.

[23] M. Buettner, A. Ramirez, W. Daily, Electrical resistance tomography for imaging the spatial distribution of moisture in pavement sections, in: Structural materials technology an NDT Conference, San Diego, California, 1996.

[24] R. Du Plooy, G. Villain, S. Palma Lopes, A. Ihamouten, X. Dérobert, B. Thauvin, Electromagnetic non-destructive evaluation techniques for the monitoring of water and chloride ingress into concrete: a comparative study, Mater. Struct. 48 (1) (2015) 369–386.

[25] D. Smyl, M. Hallaji, A. Seppänen, M. Pour-Ghaz, Three dimensional electrical impedance tomography to monitor unsaturated moisture ingress in cement-based materials: Difference imaging, Transport in Porous Med. (Accepted).

[26] D. Smyl, M. Hallaji, A. Seppänen, M. Pour-Ghaz, Quantitative electrical imaging of three-dimensional moisture flow in cement-based materials, Int. J. Heat Mass Transf. (Accepted).

[27] T. Hou, J. Lynch, Electrical impedance tomographic methods for sensing strain fields and crack damage in cementitious structures, J. Intel. Mat. Syst. Str. 20 (2009) 1363–1379.

[28] K. Karhunen, A. Seppänen, A. Lehikoinen, J. Blunt, J. Kaipio, P. Monteiro, Electrical resistance tomography for assessment of cracks in concrete, ACI Mater. J. 107 (5) (2010) 523.

[29] M. Eyuboglu, O. Birgul, Y. Z. Ider, A dual modality system for high resolution-true conductivity imaging, in: Proc. XI Int. Conf. Elec. Bioimpedance (ICEBI), 2001, pp. 409–13.

[30] C. Langton, Transport through cracked concrete: literature review, Tech. rep., SRS (2012).

[31] J. Zheng, X. Zhou, Percolation of itzs in concrete and effects of attributing factors, J. Mat. Civil Eng. 19 (9) (2007) 784–790.

[32] ASTM, Standard practice for making and curing concrete test specimens in the laboratory (2006).

[33] ASTM, Standard test method for splitting tensile strength of cylindrical concrete specimens (2011).

[34] M. D. Abràmoff, P. J. Magalhães, S. J. Ram, Image processing with ImageJ, Biophotonics international 11 (7) (2004) 36–42.

[35] J. C. Russ, R. P. Woods, The image processing handbook, J. Comput. Assist. Tomo. 19 (6) (1995) 979–981.

[36] M. Pour-Ghaz, J. Weiss, Detecting the time and location of cracks using electrically conductive surfaces, Cement Concrete Comp. 33 (1) (2011) 116–123.

[37] K. Karhunen, A. Seppänen, A. Lehikoinen, P. J. Monteiro, J. P. Kaipio, Electrical resistance tomography imaging of concrete, Cement and Concrete Res. 40 (1) (2010) 137–145.

[38] L. Borcea, Electrical impedance tomography, Inverse Probl. 18 (2002) R99–R136.

[39] P. Vauhkonen, Image reconstruction in three-dimensional electrical impedance tomography, Ph.D. thesis, University of Kuopio (2004).

[40] M. Hallaji, A. Seppänen, M. Pour-Ghaz, Electrical impedance tomography-based sensing skin for quantitative imaging of damage in concrete, Smart Mater. Struct. 23 (8) (2014) 085001.

[41] D. Liu, V. Kolehmainen, S. Siltanen, A. Laukkanen, A. Seppänen, Estimation of conductivity changes in a region of interest with electrical impedance tomography, Inverse Probl. Imag. 9(1) (2015) 211–229.

[42] K.-S. Cheng, D. Isaacson, J. Newell, D. Gisser, Electrode models for electric current computed tomography, IEEE T. Bio-Med. Eng. 36 (9) (1989) 918–924.

[43] E. Somersalo, M. Cheney, D. Isaacson, Existence and uniqueness for electrode models for electric current computed tomography, SIAM Jour. on Appl. Math. 52 (4) (1992) 1023–1040.

[44] M. Vauhkonen, W. Lionheart, L. Heikkinen, P. Vauhkonen, J. Kaipio, A MATLAB package for the EIDORS project to reconstruct two-dimensional EIT images, Physiol. Meas. 22 (2001) 107–111.

[45] P. J. Vauhkonen, M. Vauhkonen, T. Savolainen, J. P. Kaipio, Three-dimensional electrical impedance tomography based on the complete electrode model, IEEE T. Biomedical Eng. 46(9) (1999) 1150–1160.

[46] J. Kaipio, E. Somersalo, Statistical and Computational Inverse Problems, Springer New York, 2005.

[47] M. Heidary-Fyrozjaee, Control of displacement fronts in porous media by flow rate partitioning, Ph.D. thesis, University of Southern California, Los Angeles, CA (2008).

[48] A. Beck, A. Ben-tal, On the solution of the tikhonov regularization of the least squares problem, SIAM J. of Optimiz. 17(1) (2006) 98–118.

[49] M. Vauhkonen, P. Vadász, E. Karjalainen, E. Somersalo, J. Kaipio, Tikhonov regularization and prior information in electrical impedance tomography, I. S. Miomed. Imaging 17(2) (1998) 285–293.

[50] D. L. Phillips, A technique for the numerical solution of certain integral equations of the first kind, Journal of the ACM (JACM) 9 (1) (1962) 84–97.

[51] J. Kaipio, V. Kolehmainen, M. Vauhkonen, E. Somersalo, Inverse problems with structural prior information, Inverse Probl. 15 (1999) 713–729.

[52] K. Karhunen, A. Seppanen, J. P. Kaipio, Adaptive meshing approach to identification of cracks with electrical impedance tomography., Inverse Probl. Imag. 8 (1).

[53] A. Adler, W. R. Lionheart, Uses and abuses of EIDORS: an extensible software base for EIT, Physiol Meas 27 (5) (2006) S25.

[54] N. Polydorides, W. Lionheart, A MATLAB toolkit for three-dimensional electrical impedance tomography: a contribution to the electrical impedance and diffuse optical reconstruction software project, Meas. Sci. Technol. 13 (12) (2002) 1871–1883.

[55] J. W. Demmel, J. R. Gilbert, X. S. Li, An asynchronous parallel supernodal algorithm for sparse gaussian elimination, SIAM J. Matrix Anal. A. 20(4) (1999) 915–952.

[56] B. J. Christensen, T. Coverdale, R. A. Olson, S. J. Ford, E. J. Garboczi, H. M. Jennings, T. O. Mason, Impedance spectroscopy of hydrating cement-based materials: Measurement, interpretation, and application, J. Am. Ceram. Soc. 77 (11) (1994) 2789–2804.

[57] S. Tang, Z. Li, H. Shao, E. Chen, Characterization of early-age hydration process of cement pastes based on impedance measurement, Constr. Build Mater. 68 (2014) 491–500.

[58] F. E. Botros, Y. S. Onsoy, T. R. Ginn, T. Harter, Richards equation–based modeling to estimate flow and nitrate transport in a deep alluvial vadose zone, Vadose Zone J. 11 (4).

[59] L. A. Richards, Capillary conduction of liquids through porous mediums, Physics 1(5) (1931) 318–333.

[60] G. W. Scherer, Poromechanics analysis of a flow-through permeameter with entrapped air, Cement Concrete Res. 38 (3) (2008) 368–378.

[61] F. Ghasemzadeh, R. Rashetnia, D. Smyl, M. Pour-Ghaz, A comparison of methods to evaluate mass transport in damaged mortar, Cement Concrete Comp. 70 (2016) 119–129.

[62] J. Castro, D. Bentz, J. Weiss, Effect of sample conditioning on the water absorption of concrete, Cement and Concrete Comp. 33 (8) (2011) 805–813.

[63] N. S. Martys, C. F. Ferraris, Capillary transport in mortars and concrete, Cement Concrete Res. 27 (5) (1997) 747–760.

[64] Y. Mualem, A new model for predicting the hydraulic conductivity of unsaturated porous media, Water Resour. Res. 12(3) (1976) 513–522.

[65] M. Pour-Ghaz, R. Spragg, J. Weiss, Moisture profiles and diffusion coefficients in mortars containing shrinkage reducing admixtures, International RILEM Conference on Use of Superabsorbent Polymers and Other New Additives in Concrete Technical University of Denmark (2010) 197–206.

[66] D. Smyl, F. Ghasemzadeh, M. Pour-Ghaz, Simulation of unsaturated moisture transport in damaged mortar and concrete, Constr. Build. Mater. (Accepted).

[67] H. Ma, D. Hou, Z. Li, Two-scale modeling of transport properties of cement paste: Formation factor, electrical conductivity and chloride diffusivity, Comp. Mater. Sci. 110 (2015) 270–280.

[68] N. Neithalath, J. Weiss, J. Olek, Characterizing enhanced porosity concrete using electrical impedance to predict acoustic and hydraulic performance, Cement and Concrete Res. 36 (11) (2006) 2074–2085.

[69] K. Kosugi, Three-parameter lognormal distribution model for soil water retention, Water Resour. Res. 30 (4) (1994) 891–901.

[70] S. Poyet, S. Charles, N. Honore, V. L'hostit, Assessment of unsaturated water transport properties in an old concrete: determination of the pore-interaction factor, Cement and Concrete Res. 41(10) (2011) 1015–1023.

[71] M. Auroy, S. Poyet, P. Le Bescop, J. M. Torrenti, T. Charpentier, M. Moskura, X. Bourbon, Impact of carbonation on unsaturated water transport properties of cement-based materials, Cement Concrete Res. 74 (2015) 44–58.

[72] M. T. van Genuchten, A closed-form equation for predicting the hydraulic conductivity of unsaturated soils, Soil Sci. Soc. Am. J. 44 (1980) 892–898.

[73] M. T. van Genuchten, D. R. Nielson, On describing and predicting the hydraulic properties of unsaturated soils, Ann. of Geophys. 3 (1985) 615–628.

[74] R. H. Brooks, A. T. Corey, Hydraulic properties of porous media and their relation to drainage design, Transactions of the ASAE 7 (1) (1964) 26–0028.

[75] Z. Zhang, M. Thiery, V. Baroghel-Bouny, Numerical modelling of moisture transfers with hysteresis within cementitious materials: Verification and investigation of the effects of repeated wetting–drying boundary conditions, Cement Concrete Res. 68 (2015) 10–23.

[76] V. Baroghel-Bouny, Water vapour sorption experiments on hardened cementitious materials. part ii: Essential tool for assessment of transport properties and for durability prediction, Cement Concrete Res. 37 (3) (2007) 438–454.

[77] M. Mainguy, O. Coussy, V. Baroghel-Bouny, Role of air pressure in drying of weakly permeable materials, J. Eng. Mech. 127 (6) (2001) 582–592.

[78] C. Leech, D. Lockington, R. Hooton, G. Galloway, G. Cowin, P. Dux, Validation of Mualem's conductivity model and prediction of saturated permeability from sorptivity, ACI Mater. J. 105 (1) (2008) 44–51.

[79] D. Smyl, F. Ghasemzadeh, M. Pour-Ghaz, Experimental and numerical investigation of unsaturated moisture transport in damaged mortar and concrete: matrix-fracture interaction and the role of matrix porosity, Cement Concrete Res. (under review).

[80] C. Villani, R. Spragg, M. Pour-Ghaz, J. Weiss, The influence of pore solutions properties on drying in cementitious materials, J. of the Am. Ceram. Soc. 97 (2014) 386–393.

[81] J. Šimůnek, M. T. van Genuchten, M. Šejna, Development and applications of the HYDRUS and STANMOD software packages and related codes, Vadose Zone J. 7 (2) (2008) 587–600.

[82] G. González, J. Huttunen, V. Kolehmainen, A. Seppänen, M. Vauhkonen, Experimental evaluation of 3d electrical impedance tomography with total variation prior, Inverse Probl. Eng 24 (8) (2016) 1411–1431.

[83] T. Vogel, H. Gerke, R. Zhang, M. T. Van Genuchten, Modeling flow and transport in a two-dimensional dual-permeability system with spatially variable hydraulic properties, J. Hydrol. 238 (1) (2000) 78–89.